



**HAL**  
open science

## Analytical model of a resonator for PCB-embedded power conversion

Yoann Pascal, Mickael Petit, Denis Labrousse, François Costa

► **To cite this version:**

Yoann Pascal, Mickael Petit, Denis Labrousse, François Costa. Analytical model of a resonator for PCB-embedded power conversion. *Mathematics and Computers in Simulation*, 2021, 184, pp.106-117. 10.1016/j.matcom.2020.06.026 . hal-03266419

**HAL Id: hal-03266419**

**<https://hal.science/hal-03266419>**

Submitted on 3 Feb 2023

**HAL** is a multi-disciplinary open access archive for the deposit and dissemination of scientific research documents, whether they are published or not. The documents may come from teaching and research institutions in France or abroad, or from public or private research centers.

L'archive ouverte pluridisciplinaire **HAL**, est destinée au dépôt et à la diffusion de documents scientifiques de niveau recherche, publiés ou non, émanant des établissements d'enseignement et de recherche français ou étrangers, des laboratoires publics ou privés.



Distributed under a Creative Commons Attribution - NonCommercial 4.0 International License

# Analytical model of a resonator for PCB-embedded power conversion

Yoann Pascal · Mickaël Petit · Denis Labrousse · François Costa

**Abstract** This study proposes a comprehensive analytical model of the magnetism, electrostatics, and loss mechanisms of a simple and economical structure with a printed circuit board-embedded magnetic component (coil, high leakage transformer, or resonator) for electric power conversion in the range 1 W – 100 W. The predictions of this model are compared to finite element simulations. A good match is obtained over a wide bandwidth (up to at least 10 MHz). The model is adapted to predict the electrical characteristics of the device used as a monolithic series-LC tank, with a resonant frequency in the MHz range. A prototype is built to prove the applicability of the model, which is intended for the design and optimisation of power electronics converters.

**Keywords:** PCB-embedding; power electronics; analytical model; magnetic component; integrated resonator; monolithic resonator

## 1 Introduction

Embedding power converters into printed circuit board (PCB) substrates can be an efficient way to increase power density, improve modularity and reliability, simplify cooling, and decrease manufacturing costs [1, 2]. In particular, various structures with PCB-based magnetic components have been studied such as 2D windings and 3D cores (e.g., racetrack, pot core) [3, 4, 5], 3D windings and 2D cores (e.g., toroid, meander) [6, 7, 8], or air-core components [9, 10, 11].

**Fig. 1-a** shows a PCB-embedded magnetic component of the first kind; it is composed of copper spirals placed between two magnetic disks. Similar structures were studied in [12, 13, 14], for example. Depending on the number of spirals, it can be used as an inductor, a high-leakage transformer, or a resonator. When manufactured using standard PCB copper traces, the copper ribbons are planar (i.e., such that  $t \ll \nu$ , **Fig. 1-a**) and this structure is at a disadvantage: the magnetic field in the air-gap is orthogonal to the traces, which induces high eddy currents and thus high AC losses. In [15], we proposed a new process (though compatible with conventional PCB manufacturing facilities) to build copper spirals with an opposite aspect ratio ( $\nu \ll t$ , **Fig. 1-b**). This change in the orientation of copper ribbons results in a substantial decrease in AC resistance. It was shown in [15] that the losses of a 28-to-12 V/4 A buck converter could then be cut by about 40 %. This first

---

Y. Pascal · M. Petit · D. Labrousse  
SATIE Laboratory, CNAM, 75003 Paris France  
E-mail: yoann.pascal@satie.ens-cachan.fr  
F. Costa  
SATIE Laboratory, Univ. Paris Est Créteil, 94000 Créteil, France



**Table 1** Parameters defining a device (cf. Fig. 1)

Parameter	
$t$	Height of the copper ribbons ( $\vec{z}$ direction)
$v$	Thickness of the copper ribbons ( $\vec{\rho}$ )
$d$	Distance between the MPs
$e$	Thickness of the MPs
$\zeta$	Distance between the middle of the outer trench turn and the edge of the MPs
$N$	Number of turns per winding
$\chi$	Spiral step
$w_t$	Width of the trench
$\rho_e$	Radius of the MPs
$\rho_i$	Mean radius of the $i^{\text{th}}$ turn
$\mu_r$	Relative permeability of the MPs
$\epsilon_t$	Permittivity of the resin filling the trench
$\epsilon_p$	Permittivity of the PCB substrate

MP: magnetic plate.

The main hypothesis of our models is that the device is axisymmetric. Each turn is therefore likened to a ring considered independently from the others. Furthermore, it is assumed that the median plane ( $\vec{z}^\perp$ ) of the device is a symmetry plane, and that the magnetic material is linear (except possibly for the core loss estimation – section 5). Even though the device is intended for power conversion, this assumption is reasonable, since the airgap is a priori long enough to keep the magnetic material from saturation.

Since a copper ribbon is deposited on each side of the machined trench, such a device has an even number of windings. The model developed hereafter considers a device with a single trench and therefore two windings, although it could easily be generalised to any even number of windings.

### 3 Magnetic model

#### 3.1. Modelling

As the structure under study is simple and highly symmetrical, it is easy to describe its magnetic properties using a distributed reluctant network. To this end, the H field is assumed to be axial in the gap and radial in the magnetic plates. A similar method can be found, for instance, in [13]. Let us consider a thin slice of the device (Fig. 2) between radii  $\rho$  and  $\rho + d\rho$  ( $d\rho \ll \rho$ ); let  $\mathcal{F}$  and  $\phi$  be the magnetic potential and flux in the magnetic plates;  $\mathcal{R}_s$  and  $\mathcal{R}_p$  are the distributed reluctance of the magnetic material and gap:

$$\mathcal{R}_s = \frac{2}{2\pi\mu_0\mu_r\rho e} \cdot d\rho, \quad \mathcal{R}_p = \frac{\tilde{d}}{2\pi\rho\mu_0} \cdot \frac{1}{d\rho} \quad (1)$$

Where:

$$\tilde{d} = d + \frac{e}{\mu_r} \approx d \quad (2)$$

Is an estimate of the effective length of the gap.

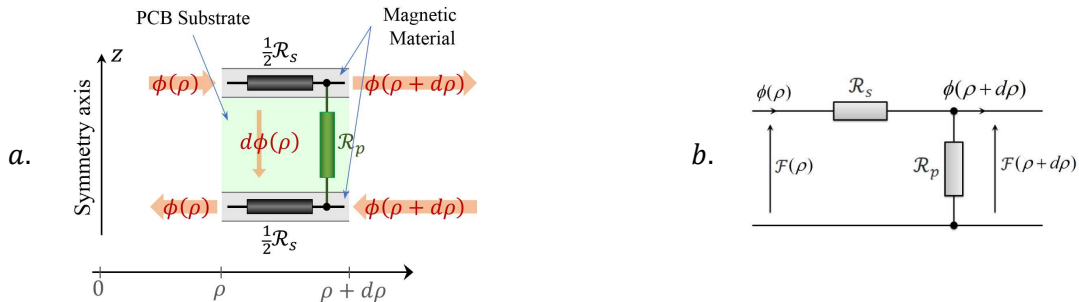


**Fig. 2** a. Section of the device under study between radii  $\rho$  and  $\rho + d\rho$ . b. Associated distributed reluctant model.

Applying Kirchhoff laws for magnetism (deduced from Maxwell equations) to this network, yields:

$$\begin{cases} \mathcal{F}(\rho + d\rho) \cdot \mathcal{R}_p(\rho)^{-1} + \phi(\rho + d\rho) = \phi(\rho) \\ \mathcal{F}(\rho) - \mathcal{F}(\rho + d\rho) = \mathcal{R}_s(\rho) \cdot \phi(\rho) \end{cases} \quad (3)$$

Hence the following modified Bessel equation:

$$x\phi'' - \phi' - x\phi = 0, \quad x = \frac{\rho}{\delta}, \quad \delta = \sqrt{\frac{\mu_r \tilde{d}e}{2}} \quad (4)$$

Its solution is:

$$\phi(x) = x \cdot (A I_1(x) + B K_1(x)) \quad (5)$$

Where  $A$  and  $B$  are constants depending on the boundary conditions, and  $I_1$  and  $K_1$  are the first-order modified Bessel functions of the second kind.

It is assumed that the excitation frequency is high enough to prevent the magnetic flux from crossing the copper track; for a first approximation, this requires the skin depth to be less than the width of the traces  $v$ , that is:

$$f > (\pi \mu_{Cu} \sigma_{Cu} v^2)^{-1} \quad (6)$$

Where  $\sigma_{Cu}$  and  $\mu_{Cu}$  are the conductivity and permeability of copper. Each copper ribbon can therefore be modelled as a lumped reluctance  $\mathcal{R}_t$  (cf. (7)) to account for the magnetic material, series-connected with a magneto-motive force (MMF) source. We have:

$$\mathcal{R}_t = \frac{1}{\pi \mu_0 \mu_r e} \cdot \ln\left(\frac{2\rho_i + v}{2\rho_i - v}\right), \quad i \in \llbracket 1, 2N \rrbracket \quad (7)$$

Where  $\rho_i$  is the mean radius of the  $i^{th}$  ribbon of copper.

(5) is then used in each space between the ribbons, and the integration constants are calculated using the continuity of  $\phi$ . This yields the magnetic flux distribution all throughout the device: i.e., in the magnetic material and the gap. The flux linkage and then the mutual inductances  $M_{s,ij}$  between the tracks  $i$  and  $j$  are then derived:

$$\forall (i, j) \in \llbracket 1, 2N \rrbracket^2, \quad M_{s,ij} = \phi(\rho_j/\delta) \cdot I_i^{-1} \quad (8)$$

Where  $I_i$  is the current flowing in the  $i^{th}$  turn. The inductance matrix  $M_w$  between the windings is finally calculated:

$$\forall (p, q) \in \llbracket 1, 2 \rrbracket^2, \quad M_{w,pq} = \sum_{i \in \mathbb{L}_p, j \in \mathbb{L}_q} M_{t,ij} \quad (9)$$

Where  $\mathbb{L}_p$  is the set of indices of the turns belonging to the winding  $p$ . For instance, in a two-winding component, the first winding comprises turns 1 to  $N$  and:

$$\mathbb{L}_1 = \llbracket 1, N \rrbracket, \quad \text{and} \quad \mathbb{L}_2 = \llbracket N + 1, 2N \rrbracket, \quad (10)$$

### 3.2. Model validation with finite element analyses

**Table 2** Ranges of the parameters used to validate the magnetic and copper loss models.

Parameter	Min. value	Max. value	Unit
$t$	0.2	4	mm
$v$	1	1000	$\mu\text{m}$
$d$	0.4	4.4	mm
$e$	0.1	2	mm
$\zeta$	0.1	52	mm
$N$	1	15	N.A.
$\chi$	0.1	14	mm
$w_t$	0.05	10	mm
$\rho_e$	5	94	mm
$\mu_r$	25	425	N.A.

$$\overline{\overline{f}} \quad \overline{1 \text{ k}} \quad \overline{10 \text{ M}} \quad \overline{\text{Hz}}$$

The inductances of devices with random parameters were estimated using both the proposed model and the FEA. The parameters of these devices were uniformly drawn in the ranges given in Table 2, while the devices that were not physically feasible (e.g., because  $\chi < w_t$ ) were discarded. Axisymmetric simulations were performed using FEMM software [16].

The statistical probability density function of the relative difference between the results is given in **Fig. 3**. It is weakly scattered, with a standard deviation of 16 percentage points. The average is non-zero: the inductance is usually underestimated. This is because the model was developed for high-frequency excitations, whereas it was tested on wideband conditions ( $f \in [1 \text{ k}, 10 \text{ M}] \text{ Hz}$ ). Furthermore, the leakage flux is not properly captured, although [17] proposes a solution to this issue. This model is nevertheless a rather good estimator of inductance, given the tolerance on the inductance of commercial coils, usually close to  $\pm 20 \%$ .

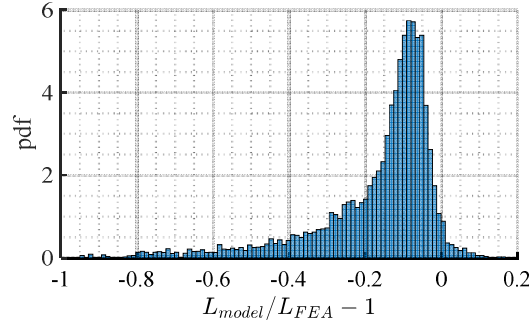


**Fig. 3** Statistical probability density function (pdf) of the relative difference between the proposed model and the FEA for the inductance; 7,000 random devices are considered.

## 4 Copper loss model

### 4.1. Model

#### 4.1.1. Method and main hypothesis

To estimate the copper loss, an ordinary differential equation (ODE) describing the electric and magnetic fields in the copper ribbons is derived from Maxwell's equations. This ODE is then integrated using H-field values obtained by the magnetic model as boundary conditions (section 3). This method is justified by the fact that although the magnetic model is quite simple, the flux density distribution along the  $\rho$  -axis is quite complex in the device. The Poynting vector corresponding to the wave generated by each copper ribbon is then calculated, from which the lost power and then the AC resistance (ACR) can be estimated.

The model is derived under sinusoidal excitation. The frequency is supposed to be high enough to validate the magnetic model but low enough to neglect the propagation effects. As a first approximation:

$$f > \frac{1}{\pi \mu_{Cu} \sigma_{Cu} v^2}, \quad f < \frac{c}{10 \sqrt{\mu_r} \cdot \rho_e} \quad (11)$$

Where  $c$  is the speed of light in vacuum.

#### 4.1.2. Derivation of the AC resistance model

##### Magnetic field in the copper ribbons

The wave equation in the copper ribbons is:

$$\Delta \vec{H} - \sigma_{Cu} \mu_{Cu} j \omega \vec{H} = 0 \quad (12)$$

Assuming that the H field is axial (along  $\vec{z}$ ) between the magnetic disks and depends solely on  $\rho$ , (12) can be simplified as follows:

$$\frac{\partial^2 H_z}{\partial \rho^2} + \frac{1}{\rho} \frac{\partial H_z}{\partial \rho} - \alpha^2 H_z = 0, \quad \alpha^2 = j \sigma_{Cu} \mu_{Cu} \omega \quad (13)$$

The solution to this ODE is:

$$H_z = AI_0(x) + BK_0(x), \quad x = \alpha\rho \quad (14)$$

Where  $I_0$  and  $K_0$  are the zero-order modified Bessel functions of the second kind, and  $(A, B)$  is a set of constants.

The H fields on each side of the  $i^{\text{th}}$  copper ribbon are then:

$$\forall i \in \llbracket 1, 2N \rrbracket, \quad \begin{pmatrix} H_z(x_{i,+}) \\ H_z(x_{i,-}) \end{pmatrix} = \begin{pmatrix} I_0(x_{i,+}) & K_0(x_{i,+}) \\ I_0(x_{i,-}) & K_0(x_{i,-}) \end{pmatrix} \begin{pmatrix} A_i \\ B_i \end{pmatrix} \quad (15)$$

$$x_{i,\pm} = \alpha \cdot (\rho_i \pm v/2)$$

Where  $x_{i,\pm}$  are the normalised abscissas of the edges of the  $i^{\text{th}}$  copper ribbon.

Due to the continuity of the tangential component of  $\vec{H}$ ,  $H_z(x_{i,\pm})$  can be estimated using the magnetic model developed in section 3. A set of constants  $(A_i, B_i)$  can then be calculated for each copper ribbon:

$$\begin{pmatrix} A_i \\ B_i \end{pmatrix} = \begin{pmatrix} I_0(x_{i,+}) & K_0(x_{i,+}) \\ I_0(x_{i,-}) & K_0(x_{i,-}) \end{pmatrix}^{-1} \begin{pmatrix} H_z(x_{i,+}) \\ H_z(x_{i,-}) \end{pmatrix}, \quad i \in \llbracket 1, 2N \rrbracket \quad (16)$$

*Electric field in the copper ribbons*

Further assuming that the electric field is orthoradial, Maxwell-Faraday's equation yields:

$$\frac{d(\rho E_\theta)}{d\rho} = -j\mu_{cu}\omega H_z \quad (17)$$

Which, together with (14), can be integrated into:

$$E_\theta = -\frac{j\omega\mu_{cu}}{\alpha} (A \cdot I_1(x) - B \cdot K_{-1}(x)), \quad x = \alpha\rho \quad (18)$$

*Poynting vector*

For the  $i^{\text{th}}$  copper ribbon, the Poynting vector is:

$$\vec{\Pi}_i = \frac{1}{2} E_\theta H_z^* \vec{e}_\rho, \quad i \in \llbracket 1, 2N \rrbracket \quad (19)$$

Then, combined with (14) and (18):

$$\vec{\Pi}_i(x) = \frac{-j\omega\mu_{cu}}{2\alpha} (A_i I_1(x) - B_i K_{-1}(x)) (A_i^* I_0(x^*) + B_i^* K_0(x^*)) \cdot \vec{e}_\rho, \quad i \in \llbracket 1, 2N \rrbracket \quad (20)$$

*Winding resistance  $ACR_p(f)$*

The real part of the flux of the Poynting vector through the surface of the  $i^{\text{th}}$  copper ribbon is the power lost in this ribbon:

$$P_i = 2\pi \cdot \Re \left( \frac{t}{\alpha} (x_{i,-} \Pi_i(x_{i,-}) - x_{i,+} \Pi_i(x_{i,+})) \right), \quad i \in \llbracket 1, 2N \rrbracket \quad (21)$$

The resistance  $ACR_{ribbon,i}$  of each copper ribbon is then obtained by dividing this power by the square of the current  $I_i$ , which flows in this  $i^{\text{th}}$  turn. The overall ACR of the  $p^{\text{th}}$  winding can then be obtained by summing the resistances of the ribbons:

$$ACR_p(f) = \sum_{i \in \mathbb{L}_p} ACR_{ribbon,i}(f) = \sum_{i \in \mathbb{L}_p} \frac{P_i}{I_i^2}, \quad p \in \llbracket 1, 2 \rrbracket \quad (22)$$

#### 4.1.3. DC compensation

Since the H-field values used to evaluate the integration constants  $(A_i, B_i)_{i \in \llbracket 1, 2N \rrbracket}$  assume high-frequency excitation, the DC resistance (DCR) of the coils cannot be accurately estimated by the model. Nevertheless, the DCR of the  $p^{\text{th}}$  winding can be easily calculated by:

$$DCR_p = \frac{2\pi}{t\sigma_{Cu}} \sum_{i \in \mathbb{L}_p} \ln \left( \frac{2\rho_i + \nu}{2\rho_i - \nu} \right)^{-1}, \quad p \in \llbracket 1, 2 \rrbracket \quad (23)$$

The two models – ACR from (22) and DCR from (23) – can then be put together to give a wideband estimate of the device resistance as follows: the ACR is offset by an amount so that the model gives the correct low-frequency (i.e., DC) resistance. Therefore, the estimator for the resistance of the  $p^{th}$  winding, valid at both high and low frequencies, is:

$$\forall f, \quad R_{eq,p}(f) = DCR_p + ACR_p(f) - ACR_p(f \rightarrow 0), \quad p \in \llbracket 1, 2 \rrbracket \quad (24)$$

In the AC domain,  $ACR \gg DCR$ , so the bias induced by this compensation method is negligible.

Other DCR compensation techniques could be used such as separating the low- and high-frequency domains and using a smooth transition between the models.

#### 4.2. Model validation with finite elements analyses

As an example, the resistances of six random coils (from the set described in section 3.2) are given in **Fig. 4**.

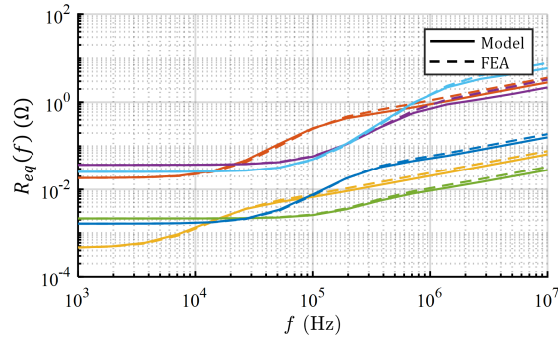


**Fig. 4** Resistances of six random coils (one coil per colour): FEA (dashed lines) and model (solid lines).

Furthermore, the resistances of one winding of each of the 7,000 devices considered in section 3.2 were estimated using the developed model (24) and the FEA. The statistical probability density function of the discrepancy between these estimations is given in **Fig. 5**. The distribution is fairly peaked on a slightly positive value, which is a conservative and valuable feature for optimisation. In particular, the resistances for 80 % of the considered devices are estimated with an error, compared to the FEA with less than 20 %. No correlation between the circuit parameters and the error could be found, and principal component analysis (PCA) did not prove useful.

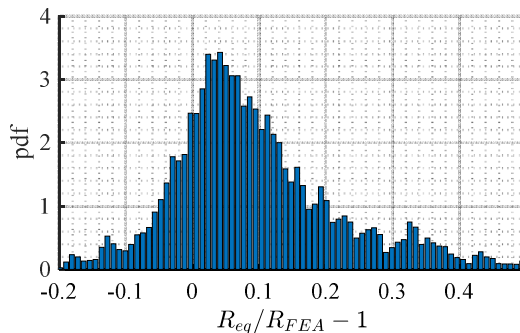


**Fig. 5** Statistical probability density function (pdf) of the relative difference between the proposed model and the FEA for copper loss in 7,000 random devices.

## 5 Core loss model

The magnetic model detailed in section 3 can be used to evaluate the magnetic field all throughout the magnetic material. Local core-loss models can then be used to estimate the power loss density  $P_d$ , which can then be integrated over the volume of the magnetic plates to obtain the overall core loss. Depending on the data

available to describe the core loss, various models can be used. Steinmetz-based equations [18] could, for instance, be used to estimate  $P_d$ . Under the small-signal assumption, the imaginary part  $\mu_r''$  of the complex-valued relative permeability can also be used [12, 19]:

$$P_d(f) = \pi f \mu_0 \mu_r'' |H_z|^2 \quad (25)$$

Due to the high airgap in the core, the magnetic material is expected to work in low-field conditions, thus rendering this formula valid even in a device intended for power conversion.

## 6 Electrostatic model

Various electrostatic models can be used, depending especially on the size of the actual device and the electrostatic properties of the magnetic material [20]. A simple generic model is used here: it assumes that each turn is only electrostatically linked to the two adjacent ones. It is further assumed that the ribbon width is high enough (i.e.,  $(w_t, \chi) < t$ ) so that fringing effects can be neglected. To increase the overall accuracy when electrostatic and magnetic models are aggregated (section 7), the capacitances are further subdivided, and the electrostatic model of the device comprises  $2N + 1$  capacitors. The capacitance linking the  $i^{th}$  turns to its neighbour through a resin-filled trench is as follows based on the formula for cylindrical capacitors:

$$\begin{aligned} C_{t,i} &= 2\pi\epsilon_t t \cdot \ln\left(\frac{\rho_i + w_t - 3v/2}{\rho_i + v/2}\right)^{-1}, \quad i \in \llbracket 1, N \rrbracket \\ C_{t,N+1} &= \pi\epsilon_t t \cdot \ln\left(\frac{\rho_N + w_t + 3(\chi - v)/4}{\rho_N + v/2 + 3\chi/4}\right)^{-1} \end{aligned} \quad (26)$$

And the capacitance linking the  $i^{th}$  turns to their neighbour through the PCB substrate is:

$$\begin{aligned} C_{p,i} &= 2\pi\epsilon_p t \cdot \ln\left(\frac{\rho_i - v/2}{\rho_i - \chi + w_t - v/2}\right)^{-1}, \quad i \in \llbracket 2, N \rrbracket \\ C_{p,N+1} &= \pi\epsilon_p t \cdot \ln\left(\frac{\rho_N - v/2 + 3\chi/4}{\rho_N - \chi/4 - w_t - v/2}\right)^{-1} \end{aligned} \quad (27)$$

## 7 LC series resonator model

### 7.1. Introduction

Due to its very geometry in which copper ribbons face each other at a short distance, the structure under study has high coupling capacitances. Along with the ribbon inductance, this parasitic element between the two copper ribbons could then be exploited to form an LC series resonant circuit. The device could then be used as a monolithic PCB-embedded resonator. In such a configuration, one connection would be made on each copper ribbon, as shown in **Fig. 6**. Other connection schemes can be considered [21], but this one has the highest power density [17].



**Fig. 6** Use of a device as an LC series resonator. Left: top view of the copper ribbons (black), their connections (red and blue), and the trench (yellow); right: equivalent circuit.

## 7.2. Equivalent circuit of the device

The magnetic, electrostatic, and copper loss models developed above consider each turn independently from the others. A quasi-distributed model with turn-level granularity can therefore be built to describe the entire device.

A partial schematic of the device is given in **Fig. 7**. The turns of the internal winding are numbered from 1 (inner turn) to  $N$  (outer turn), whereas those of the external winding are numbered from  $N + 1$  to  $2N$ . Nodes are numbered such that turn  $i \in \llbracket 1, 2N \rrbracket$  starts at node  $i$ . In **Fig. 7**, the  $i^{\text{th}}$  turn is drawn in red, whereas the volumes storing electrostatic energy associated with this turn are highlighted in pink, turquoise, violet, and beige.

The partial equivalent model is given in **Fig. 8**: the self-inductance  $L_i$  of the turn is shown in red, whereas the backgrounds of the four coupling capacitances are the same colour as those of their corresponding volume in **Fig. 7**. Other elements of the circuit are drawn in grey, whereas resistances and magnetic couplings are not shown.

The capacitances are given by (26)-(27) and the inductances by the model from section 3.

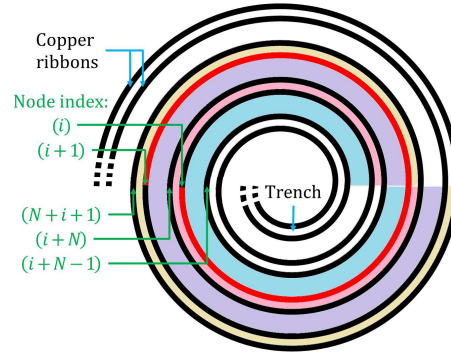


**Fig. 7** Top view of the copper ribbons (red and black) of a device. The four coloured areas (pink, blue, violet, and beige) correspond to the four capacitors modelling the electrostatic coupling between the  $i^{\text{th}}$  copper ribbon (red) and its neighbours – see **Fig. 8**.

## 7.3. Circuit solving

Usual transmission line models cannot be used to solve this circuit due to the magnetic couplings between inductances. Further, all components are, a priori, different.

Basic circuit theory can, however, be applied to estimate the impedance between nodes  $n^{\circ}1$  and  $n^{\circ}2N$ , which are connected to an external circuit.

$6N$  linear equations were written (see **Fig. 8**):  $2N$  equations corresponding to Kirchhoff's voltage law in the loops composed of  $\{C_{P,i}, C_{t,i}, L_{i-1+N}\}_{i \in \llbracket 1, N \rrbracket}$  and  $\{C_{P,i+1}, C_{t,i}, L_i\}_{i \in \llbracket 1, N \rrbracket}$ ;  $2N$  equations corresponding to Kirchhoff's current laws at nodes  $i$ ; and  $2N$  equations linking the voltage across each inductor and the currents in the turns.

The system is put into matrix form and solved numerically, thus yielding the impedance of the resonator as a function of frequency.

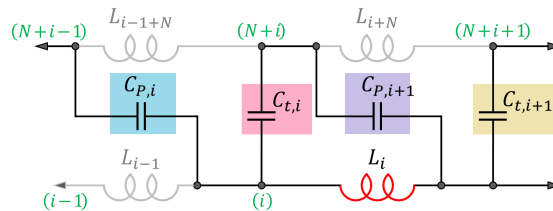


**Fig. 8** Equivalent circuit of the  $i^{\text{th}}$  copper ribbon: self-inductance (red), adjacent capacitances (black, with coloured backgrounds), and other components (grey). Green numbers between parentheses correspond to the node indexes. Resistances and magnetic couplings are not shown.

## 8 Experimental validation

### 8.1. Introduction

A prototype was manufactured and electrically characterised to compare its impedance to that predicted by the proposed model. The device was made from a polyimide substrate, and epoxy resin was used to fill the trench. Commercial magnetic sheets primarily intended for electromagnetic shielding were used, as in [4, 12, 13]. The small-signal permeability of the material (IBF15 from TDK [22]) is real ( $\mu_r = 130$ ) up to about 5 MHz, the frequency at which the magnetic loss starts to increase. The prototype has 12 turns per winding, while its overall radius and thickness are 37 mm and 2.5 mm, respectively. The sizing is detailed in Table 3 as “nominal values”.

**Table 3** Prototype sizing. (\*): parameter varied in the Monte Carlo simulations (cf. section 8.2).

Parameter		Nominal value		
$t$	Height of the copper ribbons ( $\vec{z}$ direction)	2	mm	(*)
$v$	Thickness of the copper ribbons ( $\vec{\rho}$ )	31	$\mu\text{m}$	(*)
$d$	Distance between the MPs	2.1	mm	(*)
$e$	Thickness of the MPs	180	$\mu\text{m}$	(*)
$\zeta$	Distance between the middle of the outer trench turn and the edge of the MPs	8.5	mm	(*)
$N$	Number of turns per winding	12		
$\chi$	Spiral step	1.4	mm	(*)
$w_t$	Width of the trench	0.5	mm	(*)
$\rho_e$	Radius of the MPs	37	mm	(*)
$\mu_r$	Relative permeability of the MPs	130		(*)
$\epsilon_t$	Permittivity of the resin filling the trench	3.6		
$\epsilon_p$	Permittivity of the printed circuit board substrate	3.5		

MP: magnetic plate.

### 8.2. Resistance

The resistance of one winding of the device was measured using an E4990a impedance analyser (**Fig. 9**). It remains constant up to about 100 kHz, where it starts to increase due to skin and proximity effects. Core losses dominate from around 5 MHz.

The manufacturing process was not fully mastered, so the prototype sizing was slightly different from the values given in Table 3. A Monte Carlo simulation was therefore performed to estimate the sensitivity of the resistance versus the geometrical parameters. Uniform distributions were used for all parameters marked with a star in Table 3 in a range of  $\pm 7\%$  around their nominal values, corresponding to the estimated manufacturing tolerance. The frequency dependence of complex-valued  $\mu_r$  was considered using values from the datasheet. The imaginary part of  $\mu_r$  was used to estimate the core losses. FEA showed that the peak flux density is 41 mT per ampere of resonant current. However, the self-heating of the windings limits the device current to about 500 mA<sub>rms</sub> at the resonant frequency (3.3 MHz). The magnetic material is therefore used far from saturation, and the small signal formula used to estimate the core loss (using  $\mu_r''$ , cf. (25)) is valid.

**Fig. 9** shows that resistance sensitivity is rather high, and that core loss is underestimated. This last point is probably due to the gap between the idealised geometrical model and the prototype, or to the anisotropy of the magnetic material used. This is, however, of limited impact, since the core loss increases so quickly with the frequency that no device should be designed to work in the frequency range with lossy magnetic material.

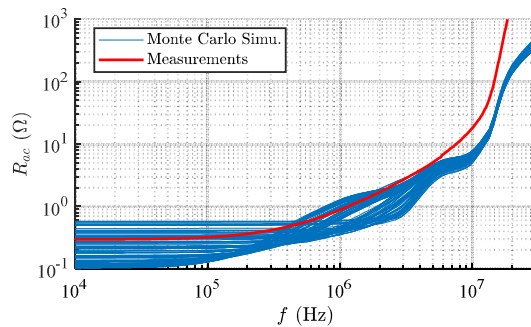


**Fig. 9** Resistance of a winding of the device: measurements (red) and Monte Carlo simulations of 84 devices (blue).

### 8.3. Impedance

The impedance of the prototype used as a resonator, both measured (using an E4990a impedance analyser) and calculated using our model, are given in **Fig. 10**. AC losses are neglected here for three reasons: 1) to reduce simulation time, 2) to separate the resistance and impedance models, and 3) because of their negligible impact on the impedance outside of the resonance. The resonator impedance and resonance frequency are well estimated, although a parasitic anti-resonance at 7.8 MHz can be seen: this is likely due to the discretisation of the model.

The size of the copper ribbons and their precise position in the airgap have little impact on the inductance. Furthermore, the impact of the inaccuracy of the process on the capacitances tends to be cancelled out (for instance, if two turns are closer to one another than average, then two others will be further apart). As a result, the impedance of the resonator can be quite accurately estimated in spite of the manufacturing inaccuracy.

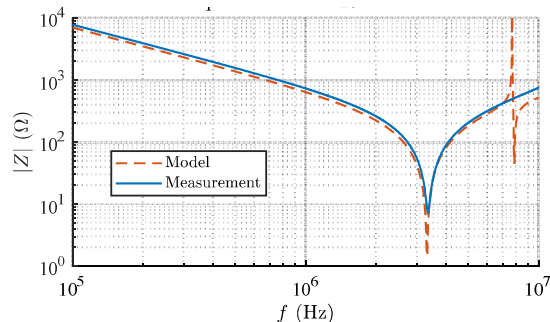


**Fig. 10** Impedance of the device used as a resonator (AC loss neglected in the model).

## 9 Conclusions

The present study considered a structure with a PCB-embedded magnetic component intended for power conversion. It can be used as an inductor, a high-leakage transformer, or a resonator. Furthermore, it is low cost and compatible with conventional PCB-manufacturing facilities.

An analytical model capturing the magnetism, electrostatics, and loss mechanisms was proposed. The predictions of the magnetic and copper loss models were compared to finite element simulations, showing a good match over a wide bandwidth. A prototype was manufactured, and its electrical characteristics were compared to those predicted by the model. This showed the value of the developed model for the design and optimisation of the structure under investigation.

### Acknowledgements

This work was supported by a grant awarded by the French National Research Agency (ANR-15-CE05-0010).

## References

- [1] K. Wang, Z. Qi, F. Li, L. Wang and X. Yang, "Review of State-of-the-Art Integration Technologies in Power Electronic Systems," *Power Electron. & Applications, IEEE Trans. on.*, vol. 2, no. 4, pp. 292-305, 2017.
- [2] PSMA, Current Developments in 3D Power Packaging with Focus on Embedded Substrate Technologies, 2015.
- [3] J. Qiu, D. V. Harburg and C. R. Sullivan, "A toroidal power inductor using radial-anisotropy thin-film magnetic material based on a hybrid fabrication process," in *IEEE Applied Power Electron. Conf. & Expo. (APEC)*, Long Beach, CA, USA, 2013.
- [4] G. Hérault, D. Labrousse, A. Mercier and S. Lefebvre, "PCB Integration of a Magnetic Component dedicated to a Power Factor Corrector Converter," in *Power Conversion & Intelligent Motion (PCIM) Europe*, Nuremberg, Germany, 2016.
- [5] R. Perrin, B. Allard, C. Buttay, N. Quentin, W. Zhang, R. Burgos, D. Boroyevic, P. Preciat and D. Martineau, "2 MHz high-density integrated power supply for gate driver in high-temperature applications," in *IEEE Applied Power Electron. Conf. & Expo. (APEC)*, Long Beach, CA, USA, 2016.
- [6] J. Serrano, I. Lope, J. Acero, C. Carretero, J. M. Burdío and R. Alonso, "Design and optimization of small inductors on extra-thin PCB for flexible cooking surfaces," *IEEE Trans. Indus. Applications*, vol. 53, no. 1, pp. 371-379, 2017.
- [7] W. Zhang, Y. Su, M. Mu, D. J. Gilham, Q. Li et F. C. Lee, «High-Density Integration of High-Frequency High-Current Point-of-Load (POL) Modules With Planar Inductors,» *Trans. on Power Electron.*, vol. 30, n° 13, 2015.
- [8] J. Biela, A. Wirthmueller, R. Waespe, M. L. Heldwein, K. Raggl et J. W. Kolar, «Passive and Active Hybrid Integrated EMI Filters,» *Trans. Power Electron.*, vol. 24, n° 15, pp. 1340-1349, 2009.
- [9] I. Lope, C. Carretero, J. Acero, J. M. Burdío and R. Alonso, "Practical issues when calculating AC losses for magnetic devices in PCB implementations," in *IEEE Applied Power Electron. Conf. & Expo. (APEC)*, Orlando, FL, USA, 2012.
- [10] Y. Nour, Z. Ouyang, A. Knott and I. H. H. Jørgensen, "Design and implementation of high frequency buck converter using multi-layer PCB inductor," in *IES, IECON*, 2016.
- [11] M. Biglarbeganian, N. Shah, I. Mazhari, J. Enslin and B. Parkhideh, "Design and evaluation of high current PCB embedded inductor for high frequency inverters," in *IEEE Applied Power Electron. Conf. & Expo.(APEC)*, 2016.
- [12] Y. Dou, Z. Ouyang, P. Thummala and M. A. E. Andersen, "PCB embedded inductor for high-frequency ZVS SEPIC converter," in *APEC*, 2018.
- [13] E. Waffenschmidt, B. Ackermann et J. A. Ferreira, «Design Method and Material Technologies for Passives in Printed Circuit Board Embedded Circuits,» *IEEE Trans. on Power Electron.*, 2005.
- [14] W. Hurley et M. Duffy, «Calculation of self and mutual impedances in planar magnetic structures,» *IEEE Trans. Mag.*, vol. 31, n° 14, 1995.
- [15] Y. Pascal, M. Petit, D. Labrousse and F. Costa, "Study of a Topology of Low-Loss Magnetic Component for PCB-Embedding," in *7th Electron. System-Integration Tech. Conf. (ESTC)*, Dresden, 2018.
- [16] D. Meeker, "Finite Element Method Magnetics, FEMM 4.2," 15 Nov. 2013. [Online]. Available: [www.femm.info](http://www.femm.info).
- [17] Y. Pascal, Étude multicritère pour l'enfouissement partiel ou total de convertisseurs d'électronique de puissance dans un circuit imprimé, Ph.D. Dissertation, ENS Paris-Saclay, 2019.
- [18] K. Venkatachalan, C. R. Sullivan, T. Abdallah and H. Tacca, "Accurate prediction of ferrite core loss with nonsinusoidal waveforms using only Steinmetz parameters," in *IEEE Proc. Workshop on Computer Power Electron.*, 2002.
- [19] M. LoBue, V. Loyau and F. Mazaleyrat, "Analysis of volume distribution of power loss in ferrite cores," *Journal of Applied Physics*, vol. 109, no. 07, p. 07D308, 2011.
- [20] A. Roesler, J. Schare and C. Hettler, "Integrated power electronics using a ferrite-based low-temperature co-fired ceramic materials system," in *Electron. Comp. Tech. Conf.*, 2010.
- [21] R. Chen, J. v. Wyk, S. Wang and W. Odendaal, "Planar electromagnetic integration technologies for integrated EMI filters," in *IAS Annual Meeting on Conf. Record of the Indus. App. Conf.*, 2003.
- [22] TDK, "Magnetic Sheets for RFID IFL/IBF series," June 2016. [Online]. Available: [product.tdk.com](http://product.tdk.com). [Accessed Janv. 2018].